

# GAUSS: Guided Encoder - Decoder Architecture for Hyperspectral Unmixing with Spatial Smoothness

D.Y.L. Ranasinghe, H.M.H.K. Weerasooriya, G.M.R.I. Godaliyadda, *Senior Member, IEEE*, M.P.B. Ekanayake, *Senior Member, IEEE*, H.M.V.R. Herath, *Senior Member, IEEE*, D. Jayasundara, L. Ramanayake, N. Senarath and D. Wickramasinghe

**Abstract**—In recent hyperspectral unmixing (HU) literature, the application of deep learning (DL) has become more prominent, especially with the autoencoder (AE) architecture. We propose a split architecture and use a pseudo-ground truth for abundances to guide the ‘unmixing network’ (UN) optimization. Preceding the UN, an ‘approximation network’ (AN) is proposed, which will improve the association between the centre pixel and its neighbourhood. Hence, it will accentuate spatial correlation in the abundances as its output is the input to the UN and the reference for the ‘mixing network’ (MN). In the Guided Encoder-Decoder Architecture for Hyperspectral Unmixing with Spatial Smoothness (GAUSS), we use one-hot encoded abundances generated through the k-means algorithm as the pseudo-ground truth to guide the UN in the initial state. Furthermore, we relieve the single-layer constraint on the MN by introducing the UN-generated abundances, in contrast to the standard AE used for HU. In the second stage of training, we introduce two variants on the pre-trained network using the GAUSS method. In GAUSS<sub>blind</sub>, we have concatenated the UN and the MN to back-propagate the reconstruction error gradients to the encoder. Then, in the GAUSS<sub>prime</sub>, reliable abundance results of a signal processing (SP) method were used as the pseudo-ground truth with the GAUSS<sub>architecture</sub>. According to quantitative and graphical results for four experimental datasets, the two GAUSS variants either transcended or equated the performance of existing HU algorithms from both DL and SP domains.

**Index Terms**—Hyperspectral unmixing, deep autoencoder, split architecture, spatial smoothness and correlation, supervised learning

## I. INTRODUCTION

Hyperspectral (HS) imaging is extensively used in earth observation satellites for various applications [1]: lithological mapping [2]–[6], environmental monitoring [7]–[9], and agricultural activities [10]–[12], since it captures more spectral information than its counterparts: multispectral and RGB imaging. However, HS images (HSIs) are of poor spatial resolution and are corrupted by noise and interference from atmospheric alterations and instrumentation imperfections [13]. Therefore, identifying the composition of a topography requires information recovery algorithms, known as unmixing algorithms.

D.Y.L. Ranasinghe, H.M.H.K. Weerasooriya, G.M.R.I. Godaliyadda, H.M.V.R. Herath, M.P.B. Ekanayake, D. Jayasundara, L. Ramanayake, N. Senarath and D. Wickramasinghe are with the Department of Electrical and Electronic Engineering, University of Peradeniya, KY 20400, Sri Lanka (email: e14273@eng.pdn.ac.lk, kavingaweerasooriya@eng.pdn.ac.lk, roshang-odd@ee.pdn.ac.lk, vijitha@eng.pdn.ac.lk, mpb.ekanayake@ee.pdn.ac.lk, e15157@eng.pdn.ac.lk, lakshitharamanayake@eng.pdn.ac.lk, neranjansenarath95@eng.pdn.ac.lk and dulanhawickramasinghe001@eng.pdn.ac.lk).

HS unmixing (HU) is a source separation technique that strives to extract the constituent source signal spectra and estimate their fractional presence in each pixel, referred to as endmembers and abundances. Over the evolution of HU techniques, numerous unmixing algorithms have been proposed for both linear and non-linear mixing models [14]–[17] under signal processing (SP) and deep learning (DL) domains. SP unmixing benefits from various algorithmic approaches [18] such as geometric [19]–[27], statistical [28]–[30], and sparse regression-based [31], [32]. In addition, non-negative matrix factorization (NMF) [33] has been profoundly used in HU for its concurrent extraction of endmembers and abundances with matrix decomposition and its adherence to fundamental constraints of the HU problem imposed by practical realities such having non-negative abundances. Variants of the NMF algorithm are present in the literature, which promote sparsity of the abundances [34], [35], independence of the endmembers [36], spatial-spectral information and piece-wise smoothness [37]–[40].

Application of DL, though nascent, is now prominent in HU due to the growing capacity in computational power, the ability to incorporate any contextual feature readily and the potentiality to extract information from unstructured data [41]. DL unmixing is frequently performed through semi-supervised or unsupervised fashion using convolutional networks [42]–[49], dense networks [50], [50]–[54], and recurrent networks [55] with the assistance of other functional layers such as pooling, regularization, and shaping. Nonetheless, most DL unmixing algorithms are structured as autoencoders (AEs) due to their resemblance to matrix decomposition applied in blind source separation techniques and their unsupervised learning capabilities.

However, AEs have limitations on the architecture when used for blind unmixing, even though AEs are widely employed in DL unmixing. In particular,

- The encoder optimization is conditioned on the decoder optimization with the end-to-end structure.
- The convergence of the encoder is slower due to the absence of a direct steering mechanism other than the decoder because of vanishing gradients.

Besides, according to the ablation studies in [42], [45], [56],

- The convolutional layers merely distil abstract spatial patterns of the HSI into the abundance maps rather than learning the association amongst the pixels.

- There is no forcing mechanism to support the spatial correlation in abundance values since the reference for the loss function is the original HSI.

Further, with the end-to-end architecture of AE for blind unmixing,

- The decoder will be limited to a single-layer network with linear activations to ensure the resemblance to matrix decomposition [57], [58].
- The non-linearity in spectral information is modelled [55], [59], [60], rather than a non-linear mixing process.

In this regard, we propose the three-network HU architecture (HUA). The proposed architecture is trained through two major stages. In the initial stage, the architecture referred to as ‘Guided Encoder-Decoder Architecture for Hyperspectral Unmixing with Spatial Smoothness’ (GAUSS) is followed. In the second stage, two variants  $GAUSS_{blind}$  and  $GAUSS_{prime}$  are introduced by altering the main architecture (GAUSS).

In GAUSS, the first two networks: the ‘approximation network’ (AN) and ‘unmixing network’ (HU), are encoders, and the ‘mixing network’ (MN) is the final network that serves as the decoder of the HUA. The AN is introduced to improve the association between the centre pixel and its neighbourhood in order to improve contextual spatial information in the abundance map. The output of the AN is compared against the actual spectral signature of the centre pixel to ensure the convergence of the network. The estimated centre pixel is used as the input to the UN. Furthermore, it is used as the output reference to compute the reconstruction error for the optimization of the MN.

Next, we investigate using a pseudo-ground truth, created by first segmenting the HSI with k-means and then converting it to a one-hot encoded representation for abundances to optimize the unmixing process of the spectral signatures. The pseudo-ground truth provides gradients for the UN to optimize its weights, untied from the decoder gradients. This opposes the conventional optimization of the unmixing process of AEs, where the unmixing optimization is conditioned on the HS pixel or image reconstruction. Hence, the pseudo-ground truth steers the output of the UN towards the latent space spanned by the actual abundances.

After initializing through the  $GAUSS_{architecture}$  in the second phase, we train the network introducing several changes to the architecture resulting in two variants with improved performance. First, inspired by [44], the untied MN will be merged with the UN in the  $GAUSS_{blind}$  method, while only allowing the encoder’s training to optimize abundances. Further, merging the UN and the MN in the second stage of training allowed the exclusion of the pseudo-ground truth. Then, in the second variant,  $GAUSS_{prime}$ , the original  $GAUSS_{architecture}$  is kept intact while being retrained with a more refined pseudo ground truth generated by a specifically selected SP algorithm [34] based on its unmixing performance.

The decoder of a typical AE architecture used in existing methods for HU is single-layered. The introduction of pseudo ground truth to train the UN prior to the training of the MN adds more flexibility to the decoder enabling the addition of more layers to it. The use of a pseudo-ground truth instills the

spatial context and basic texture of the abundance map for the UN. This training of the UN prior to MN ensures the generated abundance to be at least an approximation abundance for the corresponding pixel. The input to the MN is the output provided by the UN while its’ output is the reconstructed pixel. Hence, the functionality of the decoder is to find the layer weights which will eventually generate the spectral signature once the abundances are provided. Therefore, because of this explicit nature of the input in the proposed architectures, the decoder needs not to be confined to a single layer. Thereby, with the design flexibility of the decoder, it is not bounded to perform a merely linear unmixing. Furthermore, it provides the possibility of unmixing following a linear or a non-linear premise.

In summary, the primary contribution of this article is twofold.

- 1) Introduction of a novel architecture enabling preservation of the smoothness and spatial correlation of the local subspace structure and improving the neighboring pixels’ association with the centre pixel.

Centre pixel estimation through the neighborhood has enabled the injection of spectral correlation and smoothness of the given local environment to be inhibited into the unmixing process. This generative process ensures the functional continuity among the pixels thus ensuring spectral smoothness and continuity while subjected to the constraints of the given environment. Hence, it has the added advantage of imposing a degree of smoothness that is inherent to the given environment.

- 2) Introduction of a pseudo-ground truth at the end of the UN decouples the encoder abundance map generation process and the decoder mixing for end member generation allowing the encoder and decoder to be optimized separately.
  - a) Decoupling the dependency of abundance map generation of encoder from the decoder optimization enables the unmixing network to find the solution space separately. While the addition of a pseudo ground truth steers the learning process of the encoder towards an optimum solution, through successive training rounds more refined pseudo-ground truth can be injected to further refine the unmixing solution.
  - b) Improved flexibility of the decoder releases the single layer constraint which binds the performance of the decoder to be linear, therefore allowing the possibility of modeling the underlying non-linearity of the mixing process.

- 3) A more complex and novel synthetic data set has been created for comparison purposes which incorporates fast varying irregularities, and pure regions to emulate the environment of a real HSI. The process of generation of the synthetic data set is explained in section IV - B.

Further expanding on the capabilities of the GAUSS initializer, we proposed two variants:  $GAUSS_{blind}$  and  $GAUSS_{prime}$ , with modifications to the architecture in the former and to the pseudo-ground truth in the latter based upon the flexibility

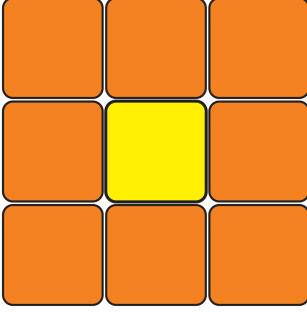


Fig. 1: Moore neighbourhood graph for the approximation network where the centre pixel is in yellow and its neighbourhood in orange

introduced by the initial training stage. The introduction of the two variants established a framework to interpret variances in unmixing performances of different HU algorithms for various HS datasets and a simulated dataset with reasonable spatial complexity. The remainder of the paper is as follows. In Section II, the concept of the GAUSS initializer and the variants are delineated followed by Section III with implementation details for the HUA. Finally, the experiments and the result comparison with competing algorithms are presented in Section IV with explanations for the exceptional performance of the two variants ascribing to the flexibility offered by GAUSS and the effective combination of different strategies for a multitude of datasets.

## II. PROBLEM FORMULATION AND THE PRINCIPLES OF THE SOLUTION

### A. Notation

Scalars are denoted by both lower ( $x$ ) and uppercase ( $X$ ) normal fonts. Boldface lowercase fonts ( $\mathbf{x}$ ) are for 1-D arrays, and 1-D arrays are ordered as column vectors. Then, boldface uppercase fonts ( $\mathbf{X}$ ) are for both 2-D and 3-D arrays.

Consider a HSI,  $\mathbf{H} \in \mathbb{R}_+^{w \times h \times B}$ , with a width and a height of  $w$  and  $h$  in pixels, respectively, and  $B$  spectral bands. The HS datacube can be rearranged as a matrix of size  $B \times N$ , where  $N$  is the total number of observations (pixels) and is the product of  $w$  and  $h$ . Accordingly, the HSI can be denoted as  $\mathbf{Y} = [\mathbf{y}_1 \cdots \mathbf{y}_j \cdots \mathbf{y}_N] \in \mathbb{R}_+^{B \times N}$  and each column  $\mathbf{y}_j \in \mathbb{R}_+^B$  is the spectrum of the  $j^{\text{th}}$  pixel. The spectral signature of the pixel at the  $(m, n)$  location of  $\mathbf{H}$  corresponds to the  $j^{\text{th}}$  column vector of  $\mathbf{Y}$ , such that  $j = \{w(m-1) + n \mid 1 < m \leq h, 1 < n \leq w\}$  where  $m$  and  $n$  is the row and column position of the pixel, respectively.

### B. Mixture Models

The linear mixture model (LMM) depends on the assumption that the incident light is reflected from the macroscopic surface only once and is measured by the sensing device of the imaging spectrometer without scattering. For its simplicity, LMM is the most frequently used model for HU in the literature [14]. The

luxury of the LMM is that a linear combination of endmember spectra can be written for each observation as

$$\mathbf{y}_j = \sum_{k=1}^K \mathbf{S}_{k,j} \mathbf{a}_k + \mathbf{e}_j \quad (1)$$

where  $\mathbf{S}_{k,j}$  is the fractional composition of the  $k^{\text{th}}$  endmember in the  $j^{\text{th}}$ ,  $\mathbf{a}_k \in \mathbb{R}_+^B$  is the spectrum of the  $k^{\text{th}}$  endmember of the HSI,  $\mathbf{e}_j \in \mathbb{R}_+^B$  is an additive disruption due to noise and modeling errors, and  $K$  is the predetermined number of endmembers in the HSI. The elements in  $\mathbf{y}_j$  and  $\mathbf{a}_k$  are non-negative as the HSI is represented using the reflectance values because it inherits atmospheric corrections and sensor independencies. Due to physical implications, the abundance non-negativity constraint (ANC)  $\mathbf{S}_{k,j} \geq 0$  and the abundance sum-to-one constraint (ASC)  $\sum_{k=1}^K \mathbf{S}_{k,j} = 1$  are imposed in 1 to assure that the fractional compositions are non-negative and the HSI only consists of the predetermined endmembers. Under the LMM, the HSI can be represented using the matrix notation as

$$\mathbf{Y} = \mathbf{A} \times \mathbf{S} + \mathbf{E} \quad (2)$$

where  $\mathbf{A} \in \mathbb{R}_+^{B \times K}$  is the endmember matrix whose columns are the spectra of each of the  $K$  endmembers,  $\mathbf{S} \in \mathbb{R}_+^{K \times N}$  is the abundance matrix with the fractional composition of each of the  $N$  pixels is organized as a column vector, and  $\mathbf{E} \in \mathbb{R}^{B \times N}$  is the noise matrix. Accordingly, the extraction of the endmember spectra ( $\mathbf{A}$ ) and their abundances ( $\mathbf{S}$ ) are the functions of HU.

When the assumptions of the LMM cannot be satisfied, a non-linear interaction between the signatures will occur. Several models have been introduced to capture the non-linear behaviour of the mixing process [61]. Intimate mixtures exploit the fact that various particles are in very close vicinity; hence, non-linear interactions between the constituents at microscopic and macroscopic levels. Due to the multipath and scattering, interactions of the photons from different sources give rise to non-linearity. Bilinear mixture models such non-linear interactions considering that order of interactions is two. Moreover, polynomial mixture models consider the within component interactions as well.

### C. Neighbourhood approximation

While the endmember spectra contain information about the spectral response of the underlying materials in the HSI, the spatial attributes of that image are stored in the abundance matrix. Therefore, in literature, to increase spatial smoothness and spatial correlation of the fractional composition, several regularization functions have been introduced in the objective function [35], [37]–[40], [62], [63] to optimize HU. However, given that the spectral signature of a given HSI is the product of the endmember spectra and its fractional abundances, the spatial correlation and smoothness could be increased using the spectral signatures of the neighbouring pixels.

If the centre pixel can be approximated from its immediate neighbourhood, then the spatial correlation and smoothness shall be established in spectral signatures, thereby in abundance values. Consider the pixel at the  $(m, n)$  location of the HSI ( $\mathbf{H}$ )

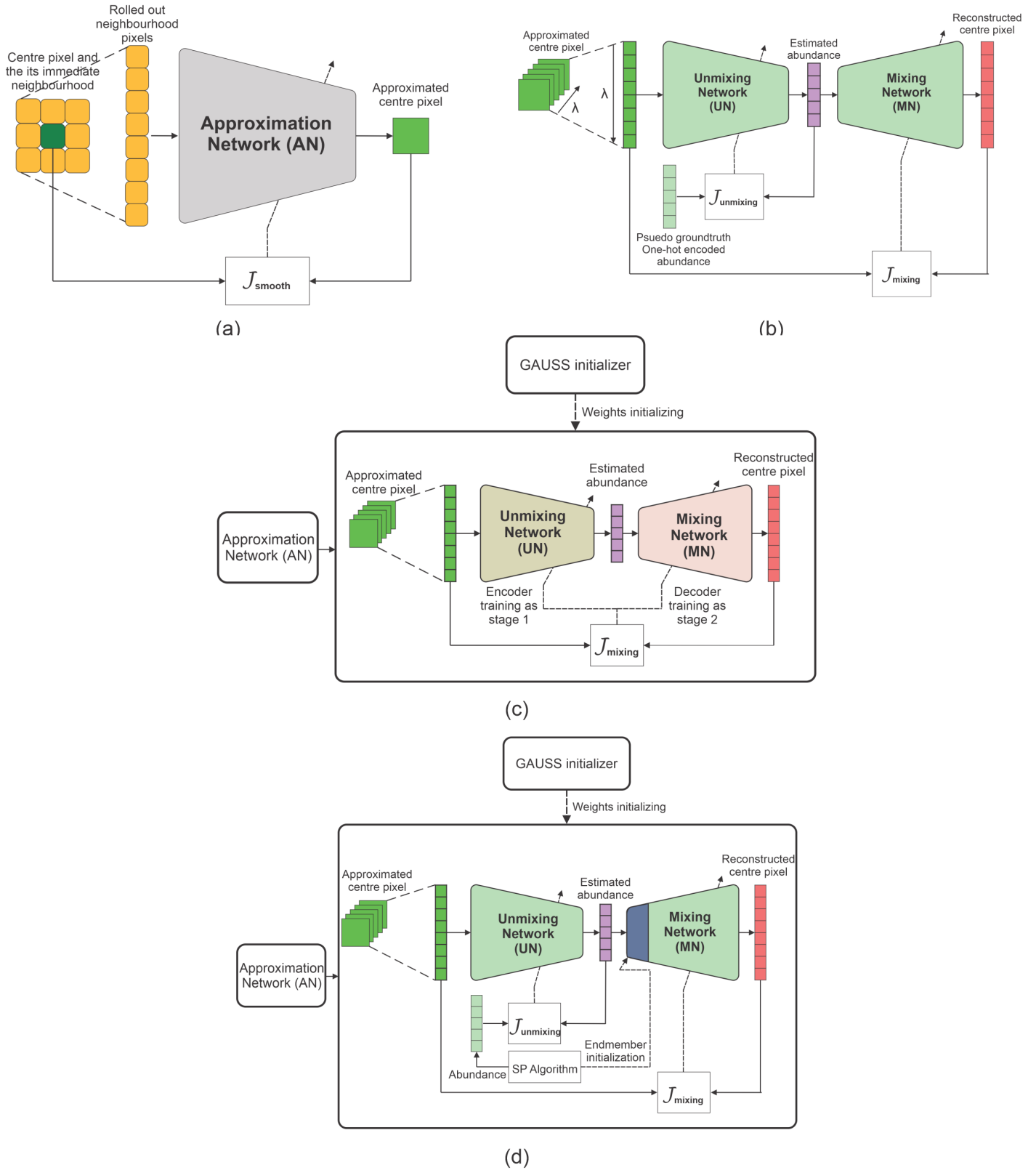


Fig. 2: (a) **GAUSS Initializer** - AN training to associate neighborhood spatial information with center pixels. (b) **GAUSS Initializer** - Sequentially trained; UN with pseudo ground truth and MN with reconstruction loss. (c) **GAUSS<sub>blind</sub>** - Sequentially trains UN then MN using the same reconstruction loss. (d) **GAUSS<sub>prime</sub>** - Sequentially trained; UN with signal processing based abundances and MN using reconstruction loss.

and the set ( $\mathcal{S}$ ) of immediate neighbourhood pixels as illustrated in Fig. 1. The set can be defined as,  $\mathcal{S} = \{\mathbf{H}_{i,j} \mid \mathbf{H}_{i,j} \in \mathbb{R}_+^B, i \in \{m-1, m+1\}, j \in \{n-1, n+1\}, i, j \in \mathbb{Z}^+\}$  and the cardinality of the set is equal to the number of neighbourhood pixels considered during the construction of the set and it is denoted by  $|\mathcal{S}|$ .

Then following the pixel to column position transition explained in Section II-A, by rearranging the vectors in  $\mathcal{S}$  as a single column vector denoted by  $\mathbf{n}_j$ , the following relationship can be formulated between the centre pixel ( $\mathbf{y}_j$ ) and its neighbourhood.

$$\mathbf{y}_j \approx \mathbf{W}_n \mathbf{n}_j \quad (3)$$

where  $\mathbf{W}_n \in \mathbb{R}^{B \times B|\mathcal{S}|}$  approximates the centre pixel using its neighbourhood pixel vector  $\mathbf{n}_j$ . To learn the spatial correlation across the HSI,  $\mathbf{W}_n$  can be trained using the following objective function,

$$\arg \min_{\mathbf{W}_n} \|\mathbf{Y} - \mathbf{W}_n \mathbf{N}\|_F^2 \quad (4)$$

Here,  $\mathbf{N}$  is the matrix constructed by concatenating the neighbour vectors of each centre pixel, and  $\mathbf{Y}$  is the matrix form of the HSI and  $\|\cdot\|_F$  is the Frobenius norm. Then by performing HU on pixels generated from the trained  $\mathbf{W}_n$  in (4), the spatial correlation and smoothness could be brought forward to fractional abundances by the AN displayed in Fig. 2.

#### D. Controlled abundance estimation

Generally, DL unmixing is performed using the AE architecture with the pixel reconstruction error as the objective function to optimize. However, a drawback of using the AE for unmixing is that it precludes direct optimization of abundances in contrast to non-DL methods. Moreover, a conventional AE architecture may suffer from the vanishing gradient problem as the network becomes deeper and deeper. That is because gradients descending through back-propagation may exponentially decrease when they reach the layers in the encoder. In addition, the unmixing process is dependent on the decoder performance of the AE because of the back-to-back connection between the encoder and the decoder.

Consequently, to avoid the dependency on the endmember signature optimization from the abundance optimization, the proposed work considers an additional objective function to train the network for abundance optimization. We create a reference for the abundance maps to train the UN, first by segmenting the HSI with k-means and converting the result to its one-hot encoded representation. This reference for the abundances is referred to as the pseudo-ground truth and is described in Section III-C. Further, the injection of a pseudo-ground truth facilitated by the split architecture provides a mechanism to reinforce the abundance optimization. It allows for a more refined pseudo-ground truth from unsupervised SP algorithms as proposed in the GAUSS<sub>prime</sub> variant (see Section III-D) for subsequent training for better accuracy.

Each pixel's fractional abundances can be considered a probability distribution with the ASC and ANC. Each abundance

value for the corresponding endmember is the individual probability. This definition allows us to reconsider the unmixing process as a classification using categorical-cross entropy as the objective function. When the UN learns hidden representations of the HSI by mapping the spectral signatures onto the probability space using the pseudo-ground truth, pixels that are not comprised of pure pixels, *i.e.* mixed pixels, will be forced towards a particular endmember. However, since the UN is a transformation on the pixel signature and the signature of a mixed pixel is different from a pure signature, the fractional abundances can be driven towards pure abundances without losing the generalization of the UN. As these two objectives behave as opposite forces, the fractional abundances will be at an equilibrium rather than driven by a single cost function.

#### E. Expanding decoder flexibility

AEs for HU are omnipresent because they resemble the matrix decomposition used in blind source separation. Since the encoder task is designed to transform the pixel or image of the HS dataset into a latent representation, there is no limitation on the number of layers in the encoder. However, unlike the encoder, the decoder of the AE does not emulate a process; instead performs the matrix multiplication between the abundances and endmembers. Therefore, the endmembers of the HS data are extracted by the weights of the decoder. Hence, the decoder architecture is bound to a single layer decoder to ensure the output of the encoder will be the abundances.

By adopting the pseudo-ground truth mechanism, the UN is trained to produce abundance values at its output in our proposed architecture independent of the decoder architectural form. Therefore, since it is guaranteed that the input of the MN is the abundances of the centre pixel, the single-layered decoder constraint can be released without using recurrent layers as in [55]. Because the output of the decoder is compared against the pixel signature, the decoder requirement is to find the optimal combination of weights that will map the abundances to spectral signatures. Further, the decoder can model the non-linear mixing process with the proposed change.

Therefore, in the GAUSS architecture, the pixel's neighbourhood is fed to the AN, and its output is compared against the actual centre pixel and the input to the UN. The UN will generate the abundances of the centre pixel at its output which is subsequently used as the input to the MN. After training, endmembers are generated by feeding an identity matrix ( $\mathbf{I} \in \mathbb{R}^{K \times K}$ ) to the MN, which represents pure pixel feeds because, with the modifications to the decoder architecture, the endmembers can no longer be extracted from the weights of the MN.

### III. METHODOLOGY

This section elaborates the proposed architecture for HU with spatial smoothness. The proposed method is primarily based on the traditional AE model used in standard HU practice under DL. However, the proposed method can be viewed as three separate networks instead of the standard AE model in HU due to the method of training adapted in this work. The architecture

of the aggregated network is illustrated in Fig. 2(a). The AN is used to impose spatial smoothness on the HSI as discussed in Section II-C. The network approximates the centre pixels  $\mathbf{Y} \in \mathbb{R}_+^{B \times N}$  using their neighbourhood pixels  $\mathbf{N} \in \mathbb{R}_+^{B|S| \times N}$  given by

$$\hat{\mathbf{Y}} = f_n(\mathbf{N}) \quad (5)$$

with  $f_n: \mathbb{R}_+^{B|S| \times N} \rightarrow \mathbb{R}_+^{B \times N}$ . The network learns the parameters for approximation by minimizing the average reconstruction error between the input  $\mathbf{Y}$  and the reconstructed spectral signatures  $\hat{\mathbf{Y}}$  from the neighbourhood pixels. Therefore, after the learning process is terminated, the smoothness matrix ( $\mathbf{W}_n$ ) in (4) and the spectral signatures with improved spatial characteristics can be realized by

$$\text{Smoothness transitions: } f_n(\mathbf{N}) \Rightarrow \mathbf{W}_n \mathbf{N} \quad (6)$$

$$\text{Smoothed pixels: } \hat{\mathbf{Y}}. \quad (7)$$

Next, to learn the hidden representation of the HSI, the UN is trained, which transforms the smoothed spectral signatures ( $\hat{\mathbf{Y}}$ ) from the AN to a low dimensional representation ( $\hat{\mathbf{L}} \in \mathbb{R}_+^{K \times N}$ ) given by

$$\hat{\mathbf{L}} = f_e(\hat{\mathbf{Y}}), \quad (8)$$

with  $f_e: \mathbb{R}_+^{B \times N} \rightarrow \mathbb{R}_+^{K \times N}$ . The output from the UN is fed to the MN, which decompresses the hidden representation to reconstruct the smoothed spectral signatures at its output. The decoder function, therefore, can be represented as

$$\hat{\mathbf{Y}} = f_d(\hat{\mathbf{L}}) \quad (9)$$

where  $f_d: \mathbb{R}_+^{K \times N} \rightarrow \mathbb{R}_+^{B \times N}$ , and  $\hat{\mathbf{Y}}$  is the output of the decoder network. After the successful termination of the learning process for HU, the unmixing results can be extracted by:

$$\begin{aligned} \text{Abundance estimation: } \hat{\mathbf{L}}^* &\Rightarrow \hat{\mathbf{S}} \\ \text{Endmember estimation: } f_d^*(\mathbf{I}_K) &\Rightarrow \hat{\mathbf{A}} \end{aligned} \quad (10)$$

where  $\mathbf{I}_K \in \mathbb{R}_+^{K \times K}$  is the identity matrix and \* denotes the optimal solution at the end of the training process.

#### A. Encoder

The encoder combines the AN and UN to improve spatial characteristics and learn hidden representations in this work. For each pixel of the HSI, we first consider its immediate neighbourhood and reconstruct the centre pixel from the set of neighbourhood pixels. Then, the output of the AN is sent to the UN to learn the unmixing process and estimate abundances. The architecture of the encoder is given in Fig. 2(a), and fully connected layer (FCNL) architecture is used in constructing the encoder.

In our work, the fractional abundances are considered probabilities, and learning hidden representations of the HSI is similar to performing a multi-class classification with the pseudo-ground truths. In our work, the encoder is designed to use

spatial information and optimize the estimation of fractional abundances without interference from the decoder optimization. To optimize the AN, we use the reconstruction error of the centre pixel from its neighbourhood as given by

$$\mathcal{J}_{\text{smooth}} = \frac{1}{N} \|\mathbf{Y} - \hat{\mathbf{Y}}\|_F^2 \quad (11)$$

where  $\|\cdot\|_F$  is the Frobenius norm. Then, to abide by the ANC and ASC, we apply the following scaling and standardization at the final layer of the UN defined as follows,

$$\hat{l}_{kj} = \frac{e^{-z_{kj}}}{\sum_{k=1}^K e^{-z_{kj}}} \quad (12)$$

where  $z_{kj}$  is the output of the  $k^{\text{th}}$  node at the final layer of the encoder prior activation and  $\hat{l}_{kj}$  is the estimated fractional abundance for the  $k^{\text{th}}$  endmember of the  $j^{\text{th}}$  column in  $\hat{\mathbf{L}}$ . The standardization to probability distributions given in 12 can be realized through *Softmax* activation function of the output layer of the encoder. Then to optimize the unmixing process of the encoder, the categorical cross-entropy is used as below,

$$\mathcal{J}_{\text{unmixing}} = -\frac{1}{N} \sum_{j,k=1}^{N,K} l_{kj} \log \hat{l}_{kj} + (1 - l_{kj}) \log(1 - \hat{l}_{kj}) \quad (13)$$

where  $l_{kj}$  are abundance values for  $k^{\text{th}}$  endmember of the  $j^{\text{th}}$  column of the pseudo-ground truth used to expedite optimization of the UN.

#### B. Decoder

An MLP-based network is adopted for the decoder in our proposed scheme, with its structure reported in Fig. 2. In this work, the decoder is designed to reconstruct the input to the UN, which comprises smoothed pixels generated from the AN of the proposed architecture. As discussed in Section III-A, with a pseudo-ground truth mechanism for abundance estimation, the decoder architecture is not restricted to a single-layered linear network; therefore, it can learn non-linear relationships as well.

The decoder of the proposed network learns non-linearity relationships between abundances and endmember signatures during the mixing process because of the introduced extension in the layers. Nevertheless, as mentioned in Section III-B, by extending the decoder layers, the extraction of the endmember signatures cannot be done through the network weights because the unmixing process is now not limited to a single layer rather laid out over a single network with multiple layers. However, since the decoder is trained by using abundances generated from the encoder network, the decoder can reconstruct the corresponding spectral signature for any abundance vector in the low dimensional space learned by the encoder. Hence, by feeding this one-hot encoded vector to the decoder at the end of weight training, the spectral information of the corresponding endmember can be extracted. For example, to find the endmember signature of the  $k^{\text{th}}$  endmember, we will construct a one-hot vector  $\mathbf{o}_k$  such that  $\mathbf{o}_k = [0, \dots, 0, 1, 0, \dots, 0]$  where the unity entry is at the  $k^{\text{th}}$  position of the vector. The vector

format implies the existence of a pure pixel containing only that end member. Hence, the resulted spectral signature of the MN is simply the corresponding endmember signature. Then by concatenating these one-hot vectors of each endmember, we can construct an identity matrix, when given to the decoder, which will output the endmember signatures of the HSI in a single attempt as presented in 10 for endmember estimation.

To train the decoder network, we diverge from the conventional practice of using the mean squared error between the encoder input  $\mathbf{Y}$  and the decoder output of each pixel  $\hat{\mathbf{Y}}$  defined as

$$\mathcal{J}_{\text{reconstruction}} = \frac{1}{NB} \|\mathbf{Y} - \hat{\mathbf{Y}}\|_F^2 \quad (14)$$

for the HSI. Rather, we adopt the pixel spectral information divergence (pSID) proposed by [64] as the reconstruction error to optimize the mixing process, which is defined by,

$$\begin{aligned} \mathcal{J}_{\text{mixing}} &= D(\hat{\mathbf{Y}} \parallel \hat{\mathbf{Y}}) + D(\hat{\mathbf{Y}} \parallel \hat{\mathbf{Y}}) \\ &= \frac{1}{N} \sum_{j,b=1}^{N,B} \left\{ q_{bj} \log \left( \frac{q_{bj}}{\hat{q}_{bj}} \right) + \hat{q}_{bj} \log \left( \frac{\hat{q}_{bj}}{q_{bj}} \right) \right\} \end{aligned} \quad (15)$$

where  $\mathbf{q}_j = \hat{\mathbf{y}}_j / \|\hat{\mathbf{y}}_j\|_1$  and  $\hat{\mathbf{q}}_j = \hat{\hat{\mathbf{y}}}_j / \|\hat{\hat{\mathbf{y}}}_j\|_1$  are the probability distribution vectors of the spectral signature of the  $j^{\text{th}}$  pixel of  $\hat{\mathbf{Y}}$  and  $\hat{\mathbf{Y}}$ , respectively. Accordingly,  $q_{bj}$  and  $\hat{q}_{bj}$  represent the probability values of the  $b^{\text{th}}$  band of the  $j^{\text{th}}$  pixel. Then,  $\|\cdot\|_1$  is 1-norm of the corresponding spectral signature. In 15,  $D(\cdot \parallel \cdot)$  is called the relative entropy between the smoothed pixels at the UN input and reconstructed pixels at the decoder output. The pSID defined by 15 can be used to measure the spectral similarity between corresponding pixel vectors in  $\hat{\mathbf{Y}}$  and  $\hat{\mathbf{Y}}$ .

### C. Pseudo-ground truth preparation for abundances

In the original GAUSS architecture, one-hot encoded representation is used as the pseudo-ground truth to guide the UN of the encoder. To construct the one-hot encoded representation of the HSI, we first segment the HSI using the k-means algorithm on the spectral signatures. Further, the injection of the pseudo-ground truth enables greater flexibility for the decoder structure and multiple opportunities for subsequent abundance generation steering through refined pseudo-ground truths as proposed below.

### D. Variants of the GAUSS algorithm

The GAUSS architecture is the foundation that uses the one-hot encoder abundances as the pseudo-ground truth. Then, we propose two architecture variants: GAUSS<sub>blind</sub> and GAUSS<sub>prime</sub>, for HU that are pre-trained using the GAUSS method. First, following [44], we will connect the decoder to the UN and remove the pseudo-ground truth. Then, we will train the network, similar to the conventional DL unmixing method, without allowing the decoder to train. This strategy will allow the unmixing process to optimize abundance results according to pixel reconstruct error defined by 15. After its completion, the decoder of the HUA will

be trained while the encoder training is withheld. For reference, this training method is called ‘GAUSS<sub>blind</sub>’ (see Fig. 2(b)).

Second, analogous to using unsupervised HU algorithms for endmember weight initialization, we consider abundance results of a SP algorithm with reliable unmixing performance as a pseudo-ground truth for HUA. This training strategy is referred to as the ‘GAUSS<sub>prime</sub>’ method (see Fig. 2(c)). The GAUSS<sub>prime</sub> method is a combination of both GAUSS and GAUSS<sub>blind</sub> strategies because and facilitates a hybrid modus operandi by fusing the best of the abilities of the other two methods. However, the output of the UN will be compared against the new pseudo-ground truth. Further, in this scheme, the encoder and the decoder will also be trained successively like in the GAUSS<sub>blind</sub> strategy. Nonetheless, the subsequent refinement in abundance optimization steering through the insertion of abundance maps generated via high-performing SP was enabled by using the pseudo-ground truth mechanism. Accordingly, we use the abundance results of the  $L_{1/2}$  NMF algorithm for all the datasets to maintain consistency even though it could be any contextual driver for abundance generation.

### E. Implementation and training of the network

The HUA was developed in TensorFlow v2 using the Google Collaboratory using default settings for optimization parameters, and the detailed architecture of the HUA is given in Table I. Then the Adam optimizer was used to optimize the three networks, and for the input-output dataset preparation, we used a batch size of 32 for each HSI dataset.

In all three training strategies, the encoder and the decoder are successively trained, and the section was trained for 25 epochs because the GAUSS<sub>blind</sub> and GAUSS<sub>prime</sub> methods are used with the network pre-trained by the GAUSS method. Accordingly, in both GAUSS<sub>blind</sub> and GAUSS<sub>prime</sub>, the HUA was first trained for 25 epochs under the GAUSS method, and another 25 epochs either with the GAUSS<sub>blind</sub> and GAUSS<sub>prime</sub> method totalled 50 epochs. Since the total number of epochs for the GAUSS method is different from that for the other two methods, the pre-trained AE was further trained for additional 25 epochs with the GAUSS method to enable fair comparison amongst the proposed three algorithms.

The pseudo-ground truth used for the GAUSS<sub>prime</sub> method was the abundance results from the  $L_{1/2}$  NMF algorithm considering its abundance performance for all three real datasets.

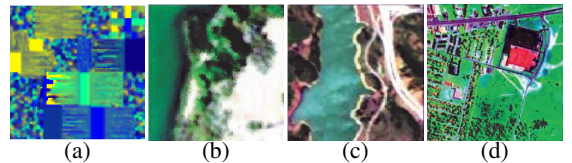


Fig. 3: RGB images of the datasets (a). Simulated (b). Samson (c). Jasper-Ridge (d). Urban

## IV. EXPERIMENTS AND DISCUSSIONS

## A. Performance criteria

The performance of the abundance estimation is measured by the average root mean square error (aRMSE), average abundance information divergence (aAID), and average abundance angle distance (aAAD). Then, the accuracy of endmember estimation from the HU algorithm is evaluated using the average spectral angle distance (aSAD) and the average spectral information divergence (aSID), which are defined as follows,

$$\text{aRMSE} = \sqrt{\frac{1}{NK} \|\mathbf{S} - \hat{\mathbf{S}}\|_F^2} \quad (16)$$

$$\text{aAAD} = \frac{1}{N} \sum_{i=j}^N \cos^{-1} \left( \frac{\langle \mathbf{s}_j, \hat{\mathbf{s}}_j \rangle}{\|\mathbf{s}_j\| \|\hat{\mathbf{s}}_j\|} \right) \quad (17)$$

$$\text{aAID} = \frac{1}{N} \sum_{j=1}^{N,K} \left\{ s_{kj} \log \left( \frac{s_{kj}}{\hat{s}_{kj}} \right) + \hat{s}_{kj} \log \left( \frac{\hat{s}_{kj}}{s_{kj}} \right) \right\} \quad (18)$$

$$\text{aSAD} = \frac{1}{K} \sum_{k=1}^K \cos^{-1} \left( \frac{\langle \mathbf{a}_k, \hat{\mathbf{a}}_k \rangle}{\|\mathbf{a}_k\| \|\hat{\mathbf{a}}_k\|} \right) \quad (19)$$

$$\text{aSID} = \frac{1}{K} \sum_{k=1}^{K,B} \left\{ p_{bk} \log \left( \frac{p_{bk}}{\hat{p}_{bk}} \right) + \hat{p}_{bk} \log \left( \frac{\hat{p}_{bk}}{p_{bk}} \right) \right\} \quad (20)$$

where  $\mathbf{S}$  and  $\hat{\mathbf{S}}$  represents the ground truth and estimated abundances. Then,  $\mathbf{s}_j$  and  $\hat{\mathbf{s}}_j$  are the ground truth and estimated abundances at  $j^{\text{th}}$  column or pixel, and  $s_{kj}$  and  $\hat{s}_{kj}$  are the ground truth and estimated abundance value for  $k^{\text{th}}$  endmember of the  $j^{\text{th}}$  pixel. Next,  $\mathbf{a}_k$  and  $\hat{\mathbf{a}}_k$  are ground truth and extracted endmember for the  $k^{\text{th}}$  source, and  $p_{bk}$  and  $\hat{p}_{bk}$  are probability value for the  $b^{\text{th}}$  spectral band of the  $k^{\text{th}}$  ground truth and extracted endmembers, respectively. The probability vector for the  $k^{\text{th}}$  endmember is computed as  $\mathbf{p}_k = \mathbf{a}_k / \|\mathbf{a}_k\|$  and  $\hat{\mathbf{p}}_k = \hat{\mathbf{a}}_k / \|\hat{\mathbf{a}}_k\|$  for the ground truth and extracted signatures, respectively.

## B. Experimental setting

To evaluate the performance of GAUSS in a complex environment an algorithm that is capable of generating simulated datasets with a sufficient amount of complexity was designed. Compared with the simulated data sets in the literature, the dimensions were selected to be  $100 \times 100$  with a spectral resolution of 198 bands.

For the generation of abundances, initially, a zeros tensor of size  $100 \times 100 \times 4$  was segmented into sixteen  $25 \times 25 \times 4$  tensors. Next, the algorithm randomly selects one from the segmented tensors and initiates the assignment of abundance fractions. This is done through a superpixel of size  $3 \times 3$ . Thereafter, a random selection of a center pixel is done and checked for occupancy. If the pixel is not already occupied then the possibility of it being on the outer edge is investigated. If the pixel is not a part of the outer edge then the superpixel of the above-mentioned dimension is constructed and the abundance fractions

TABLE I  
Network parameters of the autoencoder for unmixing

Network	Layer description	Output shape	Bias state	
Encoder	Approximation network	Input layer	[(None, $ \mathcal{S}  \times B$ )]	N/A
		Dense layer 1	(None, $\lfloor  \mathcal{S}  \times B/2 \rfloor$ )	TRUE
		Dense layer 2	(None, $\lfloor  \mathcal{S}  \times B/8 \rfloor$ )	TRUE
	Dense layer 3	(None, $B$ )	TRUE	
	Unmixing network	Input layer	[(None, $B$ )]	N/A
		Dense layer 1	(None, $\lfloor B/2 \rfloor$ )	FALSE
Dense layer 2		(None, $\lfloor B/8 \rfloor$ )	FALSE	
Decoder	Input layer	[(None, $K$ )]	N/A	
	Dense layer 1	(None, $\lfloor B/4 \rfloor$ )	FALSE	
	Dense layer 2	(None, $B$ )	FALSE	

$\lfloor \cdot \rfloor$  represents the floor operation.

are assigned while satisfying the sum to one constraint. If the selected center pixel is at an edge, then necessary alterations are done to the superpixel to get adapted according to the nature of the edge. However, following this procedure will not make the dataset realistic which contains pure regions and sparse sections as remote sense HSIs. To achieve this, some of the  $25 \times 25$  were allotted to be pure or to be to maintain a constant abundance fraction variation. This process makes sharp edges. To resolve this issue, initially, the sharp edges were extended irregularly, and then the entire image was smoothed through mean filtering. The generated image is shown in Fig. 3.

To generate the synthetic image next endmember assignment was carried out. For this, initially, four endmembers were chosen from the United States Geological Survey (USGS)<sup>1</sup> endmember library [65] was utilized. The spectral signatures of "Ilmenite, Montmorillonite, Limestone, and Tree" were chosen as the candidate endmembers. Then, as the spectral signatures extracted contained bands which were not calibrated preprocessing was carried out for the removal of not calibrated bands. Furthermore, as the spectral signatures of different elements were acquired from different sensors there was a slight deviation in the wavelengths present in each spectral signatures. To overcome this issue cubic interpolation was used to generate spectral signature containing the same wavelengths.

Moreover, a set of three real HS datasets<sup>2</sup>: Samson, Jasper-Ridge, and Urban were used for quantitative evaluation purposes. A precise ground truth for the endmembers and abundances for each dataset is available on each website. The Samson dataset consists of three endmembers with 156 spectral bands covering 401 nm to 889 nm wavelengths, while Jasper-

<sup>1</sup><https://www.usgs.gov/labs/spectroscopy-lab/science/spectral-library>

<sup>2</sup><http://lesun.weebly.com/hyperspectral-data-set.html>



Ridge comprises four sources with 198 spectral bands ranging from 380 nm to 2500 nm. The urban dataset has 162 spectral bands spanning the region from 400 nm to 2500 nm and five endmembers. The spatial resolutions of the datasets, in units of pixels  $\times$  pixels, are  $95 \times 95$ ,  $100 \times 100$  and  $307 \times 307$ , respectively.

In order to compare the results of the proposed algorithm, we have chosen eight different classical HU algorithms. In addition to DL architectures such as CNNAEU [44], DAEN [52], [57], uDAS [51] and EGU-Net [66], renowned signal processing algorithms which leverage different NMF and other geometric frameworks namely,  $L_{1/2}$  NMF [34], R-CoNMF [26], MLNMF [67], SULoRA [68] and VCA-FCLS [19] were used for this purpose. The proposed and comparison algorithms were tested on the real hyperspectral datasets as well as the simulated dataset incorporating the optimum parameters suggested by the authors in their work. The RGB images of the datasets are illustrated in Fig. 3.

### C. Experiments on simulated data

When comparing the performance of existing algorithms, signal processing-based approaches perform better than DL unmixing methods. As a whole compared to other DL methods the proposed methods have superior performance.

The conventional unmixing algorithms used in the analysis are geometry-based methods, and their derivation is based on ideal HSIs. The simulated dataset resonates with the requirement of those algorithms. The presence of pure or marginally-pure pixels favouring unmixing algorithms that exploit underlying geometric frameworks to prevail over DL unmixing algorithms is reflected through these results.

However, the results of GAUSS<sub>prime</sub> method are pre-eminent in abundance estimation. Notably, the estimated abundances of GAUSS<sub>prime</sub> have managed to be better than its pseudo-ground truth abundances from the  $L_{1/2}$  NMF algorithm. This result can be taken as evidence for the fact that the supervisory inputs used in the GAUSS<sub>prime</sub> method have contrived the abundance estimation to be accurate even for a complex environment.

With regard to end member extraction, SP based  $L_{1/2}$  NMF and RCo-NMF provide best results for aSAD and aSID error matrices respectively while the GAUSS<sub>blind</sub> has achieved the second finest result for aSID.

### D. Experiments on real data

1) *Samson dataset*: It is imperative to understand the Samson dataset to analyze the performance of the two methods. It has three principal endmembers, and the boundaries of these endmembers are almost non-overlapping. The performance of the GAUSS<sub>blind</sub> and the GAUSS<sub>prime</sub> variants is contributed by the one-hot encoded pseudo ground truth in the initial stage of the training. Similarly, by the  $L_{1/2}$  NMF pseudo ground truth in the GAUSS<sub>prime</sub> variant and the combined training of the encoder and decoder in the GAUSS<sub>blind</sub> variant during the latter stages. Consequently, the pre-training of the HUA under the GAUSS architecture has driven the optimization towards an

optimal solution space that further optimizes the reconstruction error gradients.

Next, the GAUSS<sub>prime</sub> has performed the best in terms of abundance estimation with the exception of AID. Moreover, using the  $L_{1/2}$  NMF abundances as the pseudo-ground truth, the GAUSS<sub>prime</sub> method has produced results better than the  $L_{1/2}$  NMF algorithm. The reason is that the network had benefited from pre-training the network using the GAUSS model and  $L_{1/2}$  NMF method, which has learned different properties of the latent space of the HSI. Further, the fact that GAUSS<sub>prime</sub> continues to outperform  $L_{1/2}$  NMF is a clear evidence of optimal combining, and that it is better than the GAUSS<sub>blind</sub> is because reconstruction optimization is not as effective as  $L_{1/2}$  NMF steering due to the specific landscape.

While GAUSS<sub>prime</sub> stands on top with regard to SAD, the performance of uDAS is higher when considering SID. Furthermore, the endmember performance of the GAUSS<sub>prime</sub> method has better results than that of the  $L_{1/2}$  NMF algorithm, which produced the pseudo-ground truths for the GAUSS<sub>prime</sub> method. Therefore, as the GAUSS<sub>prime</sub> method has outperformed  $L_{1/2}$  NMF algorithm in both abundance and endmember performances, the performance increment should be from combining the best attributes of the GAUSS initializer and the  $L_{1/2}$  NMF. The injection of conventional SP as a supervisory input has managed to generate a significant performance boost in HU compared to pure DL methods. This validates the combining of the two domains which has been done in the GAUSS<sub>prime</sub> architecture which is made possible by the introduction of the supervisory ground truth for UN training by the GAUSS architecture. Consequently, the decoder of the GAUSS<sub>prime</sub> method has benefited from using the AN in the HUA and the pseudo-ground truth from the  $L_{1/2}$  NMF algorithm. Since the AN improves the association between the neighboring pixels and the centre pixel, the sparsity in the HSI resulted from the direct impact of the  $L_{1/2}$  NMF algorithm will be complemented. As the output of the encoder is fed to the decoder and its output is compared against the pixels that promote sparsity in the image, the decoder benefits from the properties used by other unmixing algorithms. This combination of different aspects of algorithms via dedicated networks signifies the use of the AN and a pseudo-ground truth, as proposed in this work.

2) *Jasper-ridge dataset*: The Jasper-ridge dataset has four endmembers, and their boundaries are not as non-overlapping as in the Samson dataset.

GAUSS<sub>prime</sub> has been able to achieve the best results for abundance estimation except for the aAID error matrix. The much superior ground truth in the latter stages and the added effectiveness of the AN's spatial smoothing mechanic might have helped the proposed GAUSS<sub>blind</sub> and GAUSS<sub>prime</sub> to perform better than the other DL methods. Here, the pseudo-ground truth from the  $L_{1/2}$  NMF abundances is considered superior to the more rudimentary one-hot encoded maps used in conditioning the network through GAUSS initializer. The GAUSS initializer input information on pure or primarily pure abundances while the  $L_{1/2}$  NMF algorithm has information about abundances with lower fractions. Therefore, using the two pseudo-ground truths

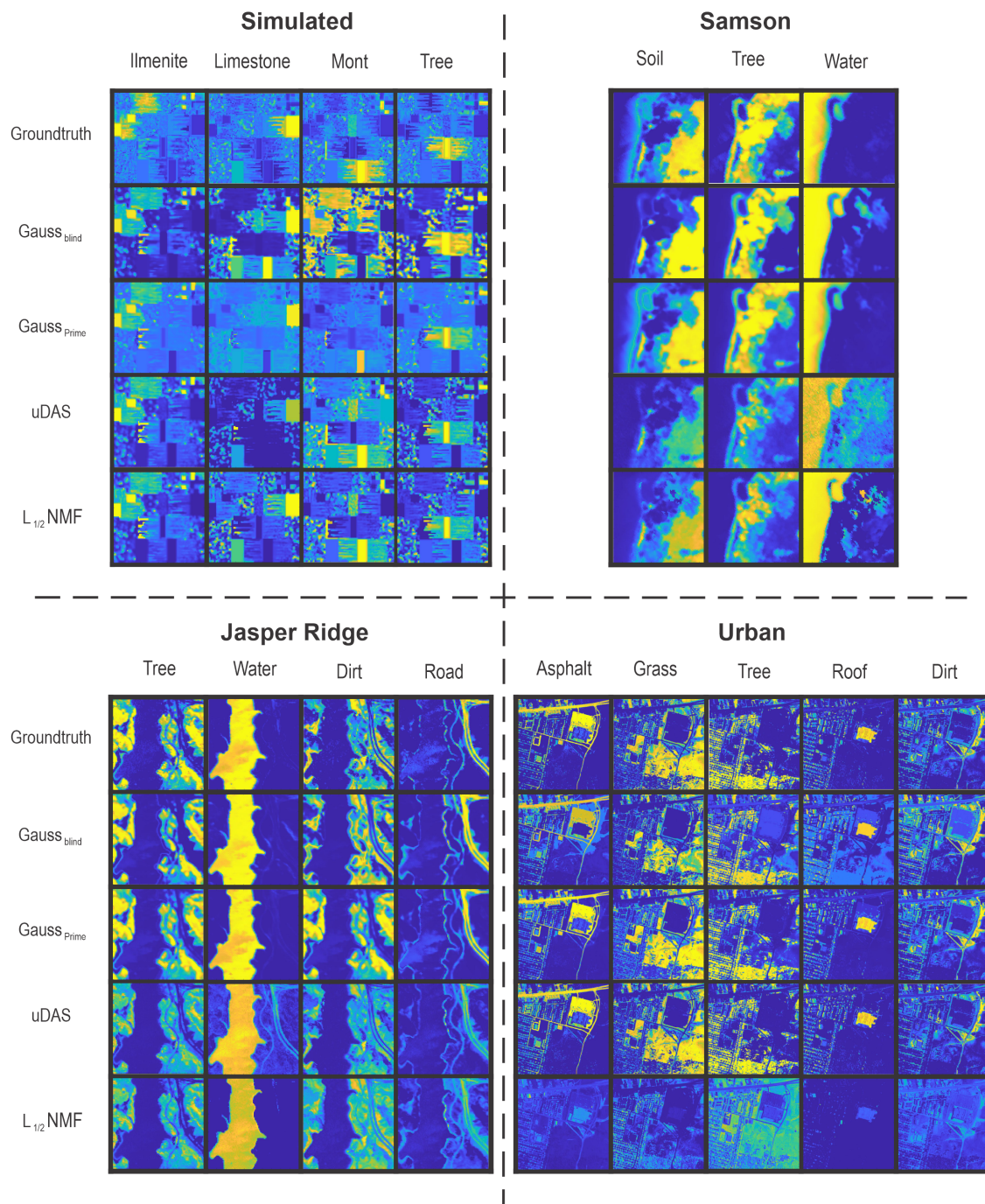


Fig. 4: Groundtruth and abundance maps for Simulated, Samson, Jasper Ridge and Urban data sets from GAUSS<sub>prime</sub>, GAUSS<sub>blind</sub>, uDAS and  $L_{1/2}$  NMF

TABLE II

Unmixing performance comparison for the four datasets: Simulated, Samson, Jasper-ridge, and Urban. The best-performing algorithms are ranked up to the third, and the ranks are superscript.

		Proposed methods		Deep learning methods				Signal processing methods					
		GAUSS <sub>blind</sub>	GAUSS <sub>prime</sub>	CNNAEU	DAEN	DAEU	EGUnet	uDAS	$L_{1/2}$ NMF	R-CoNMF	MLNMF	SULoRA	VCA FCLS
Simulated	aRMSE	0.2725	0.1312 <sup>1</sup>	0.2453	0.2550	0.2371 <sup>3</sup>	0.2783	0.2349	0.2419	0.1618 <sup>2</sup>	0.2896	0.3724	0.2874
	aAAD	0.6077	0.3414 <sup>1</sup>	0.8532	0.7386	0.8297	0.6844	0.8430	0.6909 <sup>3</sup>	0.4256 <sup>2</sup>	0.8240	0.7732	0.8168
	aAID	1.7655	0.2496	3.4171	1.5346	2.8457	2.3981 <sup>3</sup>	7.1713	2.5311	0.9826 <sup>2</sup>	3.3080	3.4135	3.9947
	aSAD	0.1325	0.2459	0.1316	0.0301	0.0756	0.1059	0.3111	0.0008 <sup>1</sup>	0.0269 <sup>3</sup>	0.0984	0.5475	0.0009 <sup>2</sup>
	aSID	0.1874 <sup>2</sup>	0.2739	0.3764	0.5461	0.3246	0.2332	0.4308	0.3436	0.0003 <sup>1</sup>	0.2467 <sup>3</sup>	1.2544	0.3433
Samson	aRMSE	0.1348 <sup>2</sup>	0.0467 <sup>1</sup>	0.3724	0.3909	0.3902	0.1573 <sup>3</sup>	0.3027	0.2689	0.3330	0.3424	0.3553	0.3996
	aAAD	0.3899	0.0724 <sup>1</sup>	0.9073	0.7774	0.8384	0.2518 <sup>2</sup>	0.5793	0.4991 <sup>3</sup>	1.0979	0.6533	0.7054	0.8825
	aAID	5.7561	4.4736 <sup>3</sup>	7.6865	6.7775	5.5561 <sup>2</sup>	1.0455 <sup>1</sup>	4.7794	4.0999 <sup>2</sup>	10.7096	6.4476	6.4119	8.0004
	aSAD	0.0345 <sup>2</sup>	0.0211 <sup>1</sup>	0.1769	0.1413	0.1155	0.0603 <sup>3</sup>	0.0697	0.0811	0.2451	0.0897	0.0990	0.1364
	aSID	0.1326	0.0584 <sup>3</sup>	1.5040	1.5217	2.4887	0.0486 <sup>2</sup>	0.0328 <sup>1</sup>	0.1953	0.4725	0.4758	0.3954	0.6746
Jasper-ridge	aRMSE	0.1224 <sup>3</sup>	0.0483 <sup>1</sup>	0.2888	0.2227	0.2623	0.4651	0.1190 <sup>2</sup>	0.3393	0.3570	0.4135	0.3494	0.4903
	aAAD	0.6732	0.1489 <sup>1</sup>	0.7186	0.5001 <sup>3</sup>	0.6239	1.2312	0.2177 <sup>2</sup>	0.8437	1.0048	1.0811	0.8596	1.2592
	aAID	12.8246	12.4485	6.8717 <sup>3</sup>	4.5497 <sup>2</sup>	7.4464	15.9190	1.5840 <sup>1</sup>	9.6208	8.6153	11.3338	10.9363 <sup>3</sup>	19.8816
	aSAD	0.0513 <sup>1</sup>	0.0965 <sup>2</sup>	0.1552	0.1328	0.1634	0.1447	0.1062	0.1677	0.1422 <sup>3</sup>	0.2241	0.1893	0.2092
	aSID	0.2126	0.1487 <sup>2</sup>	0.2635	0.2092 <sup>3</sup>	0.2710	1.3000	0.0441 <sup>1</sup>	0.8390	0.2914	1.1527	0.8440	1.3342
Urban	aRMSE	0.0912 <sup>1</sup>	0.1921 <sup>2</sup>	0.3203	0.2454	0.3777	0.5097	0.3425	0.4231	0.3330	0.4135	0.3187	0.2061 <sup>3</sup>
	aAAD	0.7321 <sup>2</sup>	2.9351	0.9947	0.7583 <sup>3</sup>	1.0989	1.4478	1.0362	1.2346	1.0979	1.0811	0.9746	0.6786 <sup>1</sup>
	aAID	14.8739	11.5265	10.2948 <sup>3</sup>	7.9027 <sup>1</sup>	12.2434	27.6442	14.9865 <sup>1</sup>	20.8305	10.7096	11.3338	14.2694	7.9499 <sup>2</sup>
	aSAD	0.0043 <sup>1</sup>	0.5814	0.2070	0.1753	0.1878	0.1351	0.0158 <sup>2</sup>	0.1258	0.2451	0.2241	0.1141	0.0956 <sup>3</sup>
	aSID	0.0231 <sup>1</sup>	0.4354 <sup>3</sup>	0.9303	1.0081	1.2864	1.3433	0.7105	0.9319	0.4725	1.1527	0.5245	0.1208 <sup>2</sup>

TABLE III

Result variances after 5 consecutive trials

		GAUSS <sub>prime</sub>	GAUSS <sub>blind</sub>
		Simulated	aRMSE
aAAD	$2.1 \cdot 10^{-4}$		$7.2 \cdot 10^{-5}$
aAID	$9.6 \cdot 10^{-5}$		$2.5 \cdot 10^{-5}$
aSAD	$6.4 \cdot 10^{-5}$		$1.4 \cdot 10^{-6}$
aSID	$7.3 \cdot 10^{-4}$		$1.7 \cdot 10^{-5}$
Samson	aRMSE	$6.35 \cdot 10^{-5}$	$4.46 \cdot 10^{-7}$
	aAAD	$2 \cdot 10^{-3}$	$5 \cdot 10^{-3}$
	aAID	$6.23 \cdot 10^{-5}$	$8.22 \cdot 10^{-5}$
	aSAD	$8.07 \cdot 10^{-5}$	$2.26 \cdot 10^{-5}$
	aSID	$5 \cdot 10^{-5}$	$7 \cdot 10^{-4}$
Jasper-ridge	aRMSE	$7.9 \cdot 10^{-5}$	$3 \cdot 10^{-4}$
	aAAD	$2 \cdot 10^{-4}$	$1 \cdot 10^{-3}$
	aAID	$4.2 \cdot 10^{-5}$	$6.3 \cdot 10^{-5}$
	aSAD	$1.2 \cdot 10^{-4}$	$3 \cdot 10^{-4}$
	aSID	$2.1 \cdot 10^{-4}$	$6.9 \cdot 10^{-3}$
Urban	aRMSE	$2.3 \cdot 10^{-4}$	$3.9 \cdot 10^{-4}$
	aAAD	$1.3 \cdot 10^{-2}$	$2.8 \cdot 10^{-2}$
	aAID	$5.3 \cdot 10^{-3}$	$4.7 \cdot 10^{-3}$
	aSAD	$7.8 \cdot 10^{-3}$	$8 \cdot 10^{-6}$
	aSID	$1.6 \cdot 10^{-2}$	$9.2 \cdot 10^{-5}$

in consecutive training stages has complemented each other in the GAUSS<sub>prime</sub> method, which reaffirms the benefits of using supervisory data to train the encoder, initially proposed for the first training stage (GAUSS architecture) with the k-means

algorithm.

In the Jasper-ridge dataset, the road endmember is challenging to extract since it is scarce compared to other endmembers and heavily correlates with the dirt endmember, despite having high reflectance values. As a result, most algorithms have not successfully extracted the road endmember, especially conventional algorithms and ultimately its abundance values. However, according to Fig. 5, all two methods in the proposed work have extracted a valid signature for the road while GAUSS<sub>blind</sub> GAUSS<sub>prime</sub> and uDAS algorithm have had the highest success. This achievement of GAUSS variants was made possible by the AN and the pseudo-ground truth. Because the AN has managed to decorrelate the pure endmembers to conform to their high correlation, and as a result, the decoder has been allowed to extract the road endmember accurately as opposed to the comparative algorithms.

3) *Urban dataset*: For the urban dataset, the GAUSS<sub>blind</sub> method has produced the best results for estimating the abundance and endmembers. Even though DAEN and VCA-FLCS have good performance in terms of aAID, GAUSS<sub>blind</sub> provides the best results for the rest matrices. Since the GAUSS variants perform unmixing pixelwise, the benefits of the spatial features in the urban HSI should be extracted by AN, which feeds its output to the UN. Also, the abundance maps for  $L_{1/2}$  NMF in Fig. 4 have much lower abundance values for most of the endmembers, and the maps have significantly deviated from the ground truths. Since there is a marked difference between the ground truth and the  $L_{1/2}$  NMF abundances, the UN in GAUSS<sub>prime</sub> has not been able to improve using a conventional algorithm with inferior performance like with the Jasper-ridge dataset. Nonetheless, it should be noted that the pseudo-ground truth of the GAUSS<sub>prime</sub> method could be any

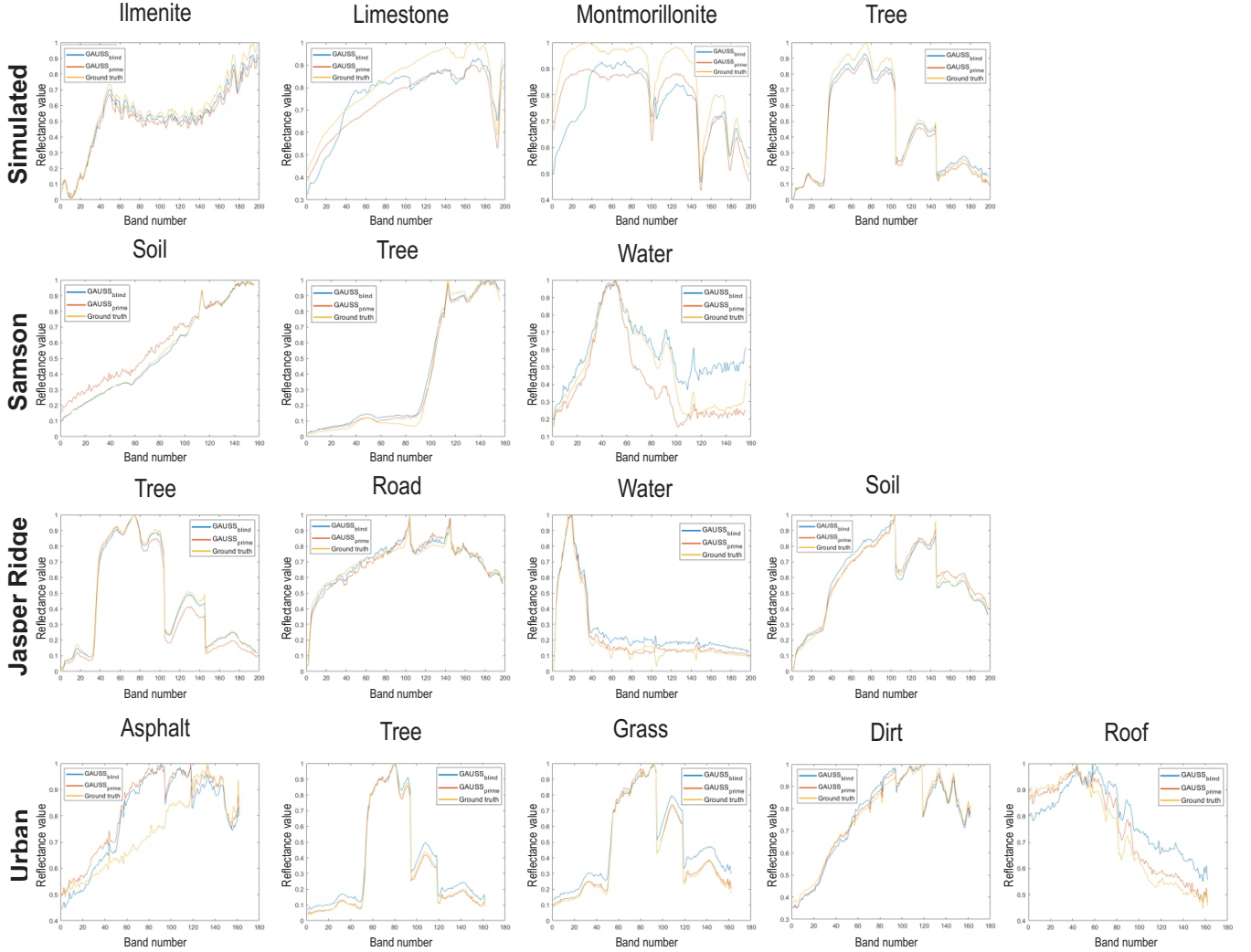


Fig. 5: Real endmember and signatures extracted for Simulated, Samson, Jasper Ridge and Urban data sets from  $GAUSS_{prime}$ ,  $GAUSS_{blind}$ , uDAS and  $L_{1/2}$  NMF

reliable SP algorithm, and the  $L_{1/2}$  NMF algorithm was used to maintain consistency among the datasets.

The  $GAUSS_{blind}$  method has the best performance for end-member extraction. Therefore, it can be said that the decoder for the  $GAUSS_{blind}$  method has already been initiated around the decoder's optimal solution after the initial training stage following the GAUSS structure. According to the aSAD metric, the endmember performance is as improved as the abundance error metric. Hence, the proposed AN and the one-hot encoded pseudo-ground truth have been conducive to endmember estimation.

According to Table II, the method with the least reconstruction error for each dataset has the best performing figures for unmixing results in Table II. Therefore, though the authors have chosen the  $L_{1/2}$  NMF algorithm as the conventional algorithm to construct a pseudo-ground truth for the training of the UN, the selection of a suitable unsupervised algorithm can also be

based on the reconstruction error of the HSI for that algorithm. However, in this work, the  $L_{1/2}$  NMF algorithm was used to maintain consistency in the comparison and remove the effect of using different algorithms in constructing the pseudo-ground truth.

### E. Summary

Even though the performance of existing SP and DL is competitive, the proposed  $GAUSS_{prime}$  and  $GAUSS_{blind}$  is comparatively superior as a whole when considering the overall results.

For sparse environments like Samson and Jasper Ridge, the performance of  $GAUSS_{prime}$  is considerably high compared to all other methods. This might be due to the presence of many pure pixels which complement the usage of k-means in the stage of training and  $L_{1/2}$  NMF in the latter stages. Further explanation can be found in section III - D.

TABLE IV  
Ablation study for the GAUSS<sub>blind</sub> method

	aRMSE	aAAD	aAID	aSAD	aSID	
Samson	AE	0.4150	0.7826	6.4259	0.1416	1.5271
	AN + AE	0.4386	0.7470	6.1648	0.1113	1.2928
	AN + pGT	0.4030	0.7241	6.2504	0.1140	0.0634
	AE + AN + pGT	0.2150	0.4350	5.9902	0.0947	0.0725
	AE + AN + GAUSS initializer + pGT	0.1348	0.3899	5.7561	0.0345	0.1326
Urban	AE	0.1793	0.7823	15.7651	0.0217	0.0288
	AN + AE	0.1158	0.8328	15.1476	0.0145	0.0286
	AN + pGT	0.1073	0.8876	15.0938	0.0074	0.3674
	AE + AN + pGT	0.0988	0.8743	15.0076	0.0106	0.0302
	AE + AN + GAUSS initializer + pGT	0.0912	0.7321	14.8739	0.0043	0.0231

TABLE V  
Ablation study for the GAUSS<sub>prime</sub> method

	aRMSE	aAAD	aAID	aSAD	aSID	
Samson	AE + pGT	0.4186	0.6975	5.4374	0.0857	0.8212
	AN + AE + pGT	0.1989	0.6183	4.1830	0.0218	0.0657
	AE + AN + GAUSS initializer + pGT	0.0467	0.0724	4.4736	0.0211	0.0584
	Urban	AE + pGT	0.3426	3.0756	11.7028	0.7006
Urban	AN + AE + pGT	0.2342	2.9588	11.9285	0.6283	0.4769
	AE + AN + GAUSS initializer + pGT	0.1921	2.9351	11.5265	0.5814	0.4354

While considering environments that are complex with sudden and scattered variations of abundances like the Urban dataset, the results have scattered among DL and SP domains equally. However, in terms of the urban dataset, the performance of the gauss blind method is noteworthy.

The consistency of performance of the introduced algorithms is assured through summarizing the results for five consecutive trials in Table II. The variances of the obtained results are illustrated in Table III

Here, AE refers to the AutoEncoder, AN refers to the Approximation Network, and pGT refers to the Pseudo ground truth.

## V. ABLATION STUDY

An ablation study has been conducted to further illustrate the effectiveness of GAUSS<sub>blind</sub> and GAUSS<sub>prime</sub> architectures on HU. Samson and Urban data sets were used for this study, and the findings are tabulated in Table IV and Table V. Furthermore, It is evident that all quantitative error metrics show the effectiveness of the two variants.

## VI. CONCLUSION

In this paper, we proposed two algorithms for HU. In this work, we discuss split training of the encoder-decoder with an additional network (AN) preceding the UN and the use of a pseudo-ground truth for abundances for supervised learning of the UN. Then, the AN approximates centre pixels from their neighborhood to improve the association between nearby pixels and spatial correlation; and performs decorrelation of pixel and endmember impurities. In addition, the use of the pseudo-ground

truth accelerated the encoder training. By releasing the single-layer constraint on the decoder it enables the possibility of modeling the underlying non-linearity of the mixing process in remote sensing and enabling subsequent training procedures with more refined abundance maps as pseudo-ground truths for improved performance. Using the pseudo-ground truth created with k-means segmentation resulted in abundance binarization, but it was conducive to estimating pure endmembers of the HSI within the initial training stage.

Based on the initial training architecture GAUSS two variants were established. In the GAUSS<sub>blind</sub>, we combine the encoder and decoder to back-propagate the reconstruction error gradients to both the decoder and the encoder. Then, in the GAUSS<sub>prime</sub> we experimented with using the abundance results of a SP-based unmixing method as the pseudo-ground truth with the combined encoder-decoder architecture, which was made possible due to the introduced pseudo-ground truth mechanic that decoupled and enabled such abundance steering. Furthermore, the use of  $L_{1/2}$  NMF allows the pathway to further expedite on using more refined pseudo-ground truth from the SP and DL domains.

The proposed variants mostly outperformed or produced results competitive with existing unmixing algorithms from DL and SP domains. In comparison with the existing DL and SP approaches for HU the performance of the proposed models can be distinguished for improved performance in terms of the considered error matrices. Besides, we discussed the effect of the dataset on the performance of the unmixing method and the selection of the unmixing algorithm out of the proposed methods for an unseen hyperspectral dataset. Meanwhile, the same technique could be applied to deciding on an algorithm to create the pseudo-ground truth.

## REFERENCES

- [1] M. J. Khan, H. S. Khan, A. Yousaf, K. Khurshid, and A. Abbas, "Modern trends in hyperspectral image analysis: A review," *Ieee Access*, vol. 6, pp. 14 118–14 129, 2018.
- [2] L. Liu, J. Feng, L. Han, J. Zhou, X. Xu, and R. Liu, "Mineral mapping using spaceborne tiangong-1 hyperspectral imagery and aster data: A case study of alteration detection in support of regional geological survey at jintanzi-malianquan area, beishan, gansu province, china," *Geological Journal*, vol. 53, pp. 372–383, 2018.
- [3] S. Lorenz, M. Kirsch, R. Zimmermann, L. Tusa, R. Möckel, M. Chamberland, and R. Gloaguen, "Long-wave hyperspectral imaging for lithological mapping: A case study," in *IGARSS 2018-2018 IEEE International Geoscience and Remote Sensing Symposium*. IEEE, 2018, pp. 1620–1623.
- [4] F. A. Kruse, J. W. Boardman, and J. F. Huntington, "Comparison of airborne hyperspectral data and eo-1 hyperion for mineral mapping," *IEEE Transactions on Geoscience and Remote Sensing*, vol. 41, no. 6, pp. 1388–1400, 2003.
- [5] L. Ni, H. Xu, and X. Zhou, "Mineral identification and mapping by synthesis of hyperspectral vnir/swir and multispectral tir remotely sensed data with different classifiers," *IEEE Journal of Selected Topics in Applied Earth Observations and Remote Sensing*, vol. 13, pp. 3155–3163, 2020.
- [6] X. Chen, J. Chen, and J. Pan, "Sulfate mineral mapping with hyperspectral imagery, a case study of the rodalquilar area, se spain," in *2019 10th Workshop on Hyperspectral Imaging and Signal Processing: Evolution in Remote Sensing (WHISPERS)*. IEEE, 2019, pp. 1–5.
- [7] M. B. Stuart, A. J. McGonigle, and J. R. Willmott, "Hyperspectral imaging in environmental monitoring: a review of recent developments and technological advances in compact field deployable systems," *Sensors*, vol. 19, no. 14, p. 3071, 2019.
- [8] D. Zeng, S. Zhang, F. Chen, and Y. Wang, "Multi-scale cnn based garbage detection of airborne hyperspectral data," *IEEE Access*, vol. 7, pp. 104 514–104 527, 2019.

- [9] M. Moroni, E. Lupo, E. Marra, and A. Cenedese, "Hyperspectral image analysis in environmental monitoring: setup of a new tunable filter platform," *Procedia Environmental Sciences*, vol. 19, pp. 885–894, 2013.
- [10] B. Lu, P. D. Dao, J. Liu, Y. He, and J. Shang, "Recent advances of hyperspectral imaging technology and applications in agriculture," *Remote Sensing*, vol. 12, no. 16, p. 2659, 2020.
- [11] M. Zhu, D. Huang, X.-J. Hu, W.-H. Tong, B.-L. Han, J.-P. Tian, and H.-B. Luo, "Application of hyperspectral technology in detection of agricultural products and food: A review," *Food Science & Nutrition*, vol. 8, no. 10, pp. 5206–5214, 2020.
- [12] M. Teke, H. S. Deveci, O. Haliloğlu, S. Z. Gürbüz, and U. Sakarya, "A short survey of hyperspectral remote sensing applications in agriculture," in *2013 6th international conference on recent advances in space technologies (RAST)*. IEEE, 2013, pp. 171–176.
- [13] B. Rasti, P. Scheunders, P. Ghamisi, G. Licciardi, and J. Chanussot, "Noise reduction in hyperspectral imagery: Overview and application," *Remote Sensing*, vol. 10, no. 3, p. 482, 2018.
- [14] R. Heylen, M. Parente, and P. Gader, "A review of nonlinear hyperspectral unmixing methods," *IEEE Journal of Selected Topics in Applied Earth Observations and Remote Sensing*, vol. 7, no. 6, pp. 1844–1868, 2014.
- [15] N. Dobigeon, J.-Y. Tourneret, C. Richard, J. C. M. Bermudez, S. McLaughlin, and A. O. Hero, "Nonlinear unmixing of hyperspectral images: Models and algorithms," *IEEE Signal processing magazine*, vol. 31, no. 1, pp. 82–94, 2013.
- [16] A. Halimi, Y. Altmann, N. Dobigeon, and J.-Y. Tourneret, "Nonlinear unmixing of hyperspectral images using a generalized bilinear model," *IEEE Transactions on Geoscience and Remote Sensing*, vol. 49, no. 11, pp. 4153–4162, 2011.
- [17] J. Gu, B. Yang, and B. Wang, "Nonlinear unmixing for hyperspectral images via kernel-transformed bilinear mixing models," *IEEE Transactions on Geoscience and Remote Sensing*, 2021.
- [18] J. M. Bioucas-Dias, A. Plaza, N. Dobigeon, M. Parente, Q. Du, P. Gader, and J. Chanussot, "Hyperspectral unmixing overview: Geometrical, statistical, and sparse regression-based approaches," *IEEE journal of selected topics in applied earth observations and remote sensing*, vol. 5, no. 2, pp. 354–379, 2012.
- [19] J. M. Nascimento and J. M. Dias, "Vertex component analysis: A fast algorithm to unmix hyperspectral data," *IEEE Transactions on Geoscience and Remote Sensing*, vol. 43, no. 4, pp. 898–910, 2005.
- [20] J. Boardman, "Automating spectral unmixing of aviris data using convex geometry concepts. summaries of the 4th annual jpl airborne geosciences workshop," *Jet Propulsion Laboratory, Pasadena, California*, 1993.
- [21] M. E. Winter, "N-findr: An algorithm for fast autonomous spectral end-member determination in hyperspectral data," in *Imaging Spectrometry V*, vol. 3753. International Society for Optics and Photonics, 1999, pp. 266–275.
- [22] L. Miao and H. Qi, "Endmember extraction from highly mixed data using minimum volume constrained nonnegative matrix factorization," *IEEE Transactions on Geoscience and Remote Sensing*, vol. 45, no. 3, pp. 765–777, 2007.
- [23] A. Zare and P. Gader, "Sparsity promoting iterated constrained endmember detection in hyperspectral imagery," *IEEE Geoscience and Remote Sensing Letters*, vol. 4, no. 3, pp. 446–450, 2007.
- [24] P. Gader, D. Dranishnikov, A. Zare, and J. Chanussot, "A sparsity promoting bilinear unmixing model," in *2012 4th Workshop on Hyperspectral Image and Signal Processing: Evolution in Remote Sensing (WHISPERS)*. IEEE, 2012, pp. 1–4.
- [25] L. Zhuang, C.-H. Lin, M. A. Figueiredo, and J. M. Bioucas-Dias, "Regularization parameter selection in minimum volume hyperspectral unmixing," *IEEE Transactions on Geoscience and Remote Sensing*, vol. 57, no. 12, pp. 9858–9877, 2019.
- [26] J. Li, J. M. Bioucas-Dias, A. Plaza, and L. Liu, "Robust collaborative nonnegative matrix factorization for hyperspectral unmixing," *IEEE Transactions on Geoscience and Remote Sensing*, vol. 54, no. 10, pp. 6076–6090, 2016.
- [27] J. M. Bioucas-Dias, "A variable splitting augmented lagrangian approach to linear spectral unmixing," in *2009 First workshop on hyperspectral image and signal processing: Evolution in remote sensing*. IEEE, 2009, pp. 1–4.
- [28] L. Parra, C. Spence, P. Sajda, A. Ziehe, and K.-R. Müller, "Unmixing hyperspectral data," *Advances in neural information processing systems*, vol. 12, 1999.
- [29] N. Dobigeon, S. Moussaoui, M. Coulon, J.-Y. Tourneret, and A. O. Hero, "Joint bayesian endmember extraction and linear unmixing for hyperspectral imagery," *IEEE Transactions on Signal Processing*, vol. 57, no. 11, pp. 4355–4368, 2009.
- [30] J. M. Nascimento and J. M. Bioucas-Dias, "Hyperspectral unmixing algorithm via dependent component analysis," in *2007 IEEE International Geoscience and Remote Sensing Symposium*. IEEE, 2007, pp. 4033–4036.
- [31] J. M. Bioucas-Dias and M. A. Figueiredo, "Alternating direction algorithms for constrained sparse regression: Application to hyperspectral unmixing," in *2010 2nd Workshop on Hyperspectral Image and Signal Processing: Evolution in Remote Sensing*. IEEE, 2010, pp. 1–4.
- [32] M.-D. Iordache, J. M. Bioucas-Dias, and A. Plaza, "Total variation spatial regularization for sparse hyperspectral unmixing," *IEEE Transactions on Geoscience and Remote Sensing*, vol. 50, no. 11, pp. 4484–4502, 2012.
- [33] D. D. Lee and H. S. Seung, "Algorithms for non-negative matrix factorization," in *Advances in neural information processing systems*. MIT Press, 2000, p. 535–541.
- [34] Y. Qian, S. Jia, J. Zhou, and A. Robles-Kelly, "L1/2 sparsity constrained nonnegative matrix factorization for hyperspectral unmixing," in *2010 International conference on digital image computing: techniques and applications*. IEEE, 2010, pp. 447–453.
- [35] W. He, H. Zhang, and L. Zhang, "Total variation regularized reweighted sparse nonnegative matrix factorization for hyperspectral unmixing," *IEEE Transactions on Geoscience and Remote Sensing*, vol. 55, no. 7, pp. 3909–3921, 2017.
- [36] E. Ekanayake, H. Weerasooriya, D. Ranasinghe, S. Herath, B. Rathnayake, G. Godaliyadda, M. Ekanayake, and H. Herath, "Constrained nonnegative matrix factorization for blind hyperspectral unmixing incorporating end-member independence," *IEEE Journal of Selected Topics in Applied Earth Observations and Remote Sensing*, vol. 14, pp. 11 853–11 869, 2021.
- [37] X. Sun, Q. Peng, B. Zhang, L. Gao, and L. Yang, "Constraint non-negative matrix factorization with sparseness and piece wise smoothness for hyperspectral unmixing," in *2018 9th Workshop on Hyperspectral Image and Signal Processing: Evolution in Remote Sensing (WHISPERS)*. IEEE, 2018, pp. 1–5.
- [38] S. Yang, X. Zhang, Y. Yao, S. Cheng, and L. Jiao, "Geometric nonnegative matrix factorization (gnmf) for hyperspectral unmixing," *IEEE Journal of Selected Topics in Applied Earth Observations and Remote Sensing*, vol. 8, no. 6, pp. 2696–2703, 2015.
- [39] B. Rathnayake, E. Ekanayake, K. Weerakoon, G. Godaliyadda, M. Ekanayake, and H. Herath, "Graph-based blind hyperspectral unmixing via nonnegative matrix factorization," *IEEE Transactions on Geoscience and Remote Sensing*, vol. 58, no. 9, pp. 6391–6409, 2020.
- [40] L. Zhou, X. Zhang, J. Wang, X. Bai, L. Tong, L. Zhang, J. Zhou, and E. Hancock, "Subspace structure regularized nonnegative matrix factorization for hyperspectral unmixing," *IEEE Journal of Selected Topics in Applied Earth Observations and Remote Sensing*, vol. 13, pp. 4257–4270, 2020.
- [41] A. Signoroni, M. Savardi, A. Baronio, and S. Benini, "Deep learning meets hyperspectral image analysis: A multidisciplinary review," *Journal of Imaging*, vol. 5, no. 5, p. 52, 2019.
- [42] L. Qi, J. Li, Y. Wang, M. Lei, and X. Gao, "Deep spectral convolution network for hyperspectral image unmixing with spectral library," *Signal Processing*, vol. 176, p. 107672, 2020.
- [43] X. Zhang, Y. Sun, J. Zhang, P. Wu, and L. Jiao, "Hyperspectral unmixing via deep convolutional neural networks," *IEEE Geoscience and Remote Sensing Letters*, vol. 15, no. 11, pp. 1755–1759, 2018.
- [44] B. Palsson, M. O. Ulfarsson, and J. R. Sveinsson, "Convolutional autoencoder for spectral-spatial hyperspectral unmixing," *IEEE Transactions on Geoscience and Remote Sensing*, vol. 59, no. 1, pp. 535–549, 2020.
- [45] Y. Ranasinghe, S. Herath, K. Weerasooriya, M. Ekanayake, R. Godaliyadda, P. Ekanayake, and V. Herath, "Convolutional autoencoder for blind hyperspectral image unmixing," in *2020 IEEE 15th International Conference on Industrial and Information Systems (ICIIS)*. IEEE, 2020, pp. 174–179.
- [46] M. Wang, M. Zhao, J. Chen, and S. Rahardja, "Nonlinear unmixing of hyperspectral data via deep autoencoder networks," *IEEE Geoscience and Remote Sensing Letters*, vol. 16, no. 9, pp. 1467–1471, 2019.
- [47] M. Zhao, M. Wang, J. Chen, and S. Rahardja, "Hyperspectral unmixing for additive nonlinear models with a 3-d-cnn autoencoder network," *IEEE Transactions on Geoscience and Remote Sensing*, 2021.
- [48] M. Zhao, S. Shi, J. Chen, and N. Dobigeon, "A 3d-cnn framework for hyperspectral unmixing with spectral variability," *IEEE Transactions on Geoscience and Remote Sensing*, 2022.
- [49] Y. Fang, Y. Wang, L. Xu, R. Zhuo, A. Wong, and D. A. Clausi, "Bcun: Bayesian fully convolutional neural network for hyperspectral spectral

- unmixing,” *IEEE Transactions on Geoscience and Remote Sensing*, pp. 1–1, 2022.
- [50] S. Ozkan, B. Kaya, and G. B. Akar, “Endnet: Sparse autoencoder network for endmember extraction and hyperspectral unmixing,” *IEEE Transactions on Geoscience and Remote Sensing*, vol. 57, no. 1, pp. 482–496, 2018.
- [51] Y. Qu and H. Qi, “udas: An untied denoising autoencoder with sparsity for spectral unmixing,” *IEEE Transactions on Geoscience and Remote Sensing*, vol. 57, no. 3, pp. 1698–1712, 2018.
- [52] Y. Su, J. Li, A. Plaza, A. Marinoni, P. Gamba, and S. Chakraborty, “Daen: Deep autoencoder networks for hyperspectral unmixing,” *IEEE Transactions on Geoscience and Remote Sensing*, vol. 57, no. 7, pp. 4309–4321, 2019.
- [53] Z. Han, D. Hong, L. Gao, B. Zhang, and J. Chanussot, “Deep half-siamese networks for hyperspectral unmixing,” *IEEE Geoscience and Remote Sensing Letters*, vol. 18, no. 11, pp. 1996–2000, 2020.
- [54] D. Hong, L. Gao, J. Yao, N. Yokoya, J. Chanussot, U. Heiden, and B. Zhang, “Endmember-guided unmixing network (egu-net): A general deep learning framework for self-supervised hyperspectral unmixing,” *IEEE Transactions on Neural Networks and Learning Systems*, 2021.
- [55] M. Zhao, L. Yan, and J. Chen, “Lstm-dnn based autoencoder network for nonlinear hyperspectral image unmixing,” *IEEE Journal of Selected Topics in Signal Processing*, vol. 15, no. 2, pp. 295–309, 2021.
- [56] B. Palsson, M. O. Ulfarsson, and J. R. Sveinsson, “Convolutional autoencoder for spatial-spectral hyperspectral unmixing,” in *IGARSS 2019-2019 IEEE International Geoscience and Remote Sensing Symposium*. IEEE, 2019, pp. 357–360.
- [57] B. Palsson, J. Sigurdsson, J. R. Sveinsson, and M. O. Ulfarsson, “Hyperspectral unmixing using a neural network autoencoder,” *IEEE Access*, vol. 6, pp. 25 646–25 656, 2018.
- [58] Y. Ranasinghe, S. Herath, K. Weerasooriya, M. Ekanayake, R. Godaliyadda, P. Ekanayake, and V. Herath, “Convolutional autoencoder for blind hyperspectral image unmixing,” in *2020 IEEE 15th International Conference on Industrial and Information Systems (ICIIS)*, 2020, pp. 174–179.
- [59] H. Li, R. A. Borsoi, T. Imbiriba, P. Closas, J. C. M. Bermudez, and D. Erdoğmuş, “Model-based deep autoencoder networks for nonlinear hyperspectral unmixing,” *IEEE Geoscience and Remote Sensing Letters*, vol. 19, pp. 1–5, 2022.
- [60] K. T. Shahid and I. D. Schizas, “Unsupervised hyperspectral unmixing via nonlinear autoencoders,” *IEEE Transactions on Geoscience and Remote Sensing*, vol. 60, pp. 1–13, 2022.
- [61] N. Dobigeon, Y. Altmann, N. Brun, and S. Moussaoui, “Linear and nonlinear unmixing in hyperspectral imaging,” in *Data Handling in Science and Technology*. Elsevier, 2016, vol. 30, pp. 185–224.
- [62] J. Sigurdsson, M. Ulfarsson, and J. Sveinsson, “Blind hyperspectral unmixing using total variation and  $\ell_q$  sparse regularization,” *IEEE Transactions on Geoscience and Remote Sensing*, vol. 54, pp. 1–14, 08 2016.
- [63] M.-D. Iordache, J. Bioucas-Dias, and A. Plaza, “Total variation spatial regularization for sparse hyperspectral unmixing,” *IEEE Transactions on Geoscience and Remote Sensing*, 10 2012.
- [64] C.-I. Chang, “Spectral information divergence for hyperspectral image analysis,” in *IEEE 1999 International Geoscience and Remote Sensing Symposium. IGARSS’99 (Cat. No. 99CH36293)*, vol. 1. IEEE, 1999, pp. 509–511.
- [65] R. F. Kokaly, R. N. Clark, G. A. Swayze, K. E. Livo, T. M. Hoefen, N. C. Pearson, R. A. Wise, W. M. Benz, H. A. Lowers, R. L. Driscoll, and A. J. Klein, “USGS Spectral Library Version 7,” U.S. Geological Survey, Reston, VA, Report 1035, 2017. [Online]. Available: <http://pubs.er.usgs.gov/publication/ds1035>
- [66] D. Hong, L. Gao, J. Yao, N. Yokoya, J. Chanussot, U. Heiden, and B. Zhang, “Endmember-guided unmixing network (egu-net): A general deep learning framework for self-supervised hyperspectral unmixing,” *IEEE Transactions on Neural Networks and Learning Systems*, pp. 1–14, 2021.
- [67] R. Rajabi and H. Ghassemian, “Spectral unmixing of hyperspectral imagery using multilayer nmf,” *IEEE Geoscience and Remote Sensing Letters*, vol. 12, no. 1, pp. 38–42, 2014.
- [68] D. Hong and X. X. Zhu, “Sulora: Subspace unmixing with low-rank attribute embedding for hyperspectral data analysis,” *IEEE Journal of Selected Topics in Signal Processing*, vol. 12, no. 6, pp. 1351–1363, 2018.



**D.Y.L. Ranasinghe** received the B.Sc. (Eng.) degree in electrical and electronic engineering from the University of Peradeniya, Sri Lanka, in 2020. Immediately after that, he joined the School of Engineering, Sri Lanka Technological Campus, Padukka, Sri Lanka, as a Research Assistant. He is currently working as a Research Assistant with the University of Peradeniya under a research grant from the International Development Research Centre (IDRC), Canada. He has published in IEEE JSTARS, IEEE Access, and numerous IEEE conferences. His research interests include hyperspectral and multispectral imaging, remote sensing, signal and image processing, and deep learning.



**H.M.H.K. Weerasooriya** received the B.Sc. degree in electrical and electronic engineering with a first-class honors from the University of Peradeniya, Peradeniya, Sri Lanka in 2020. He is currently an Instructor with the Department of Electronic and Electrical Engineering, University of Peradeniya. He is presently involved in the researches on hyperspectral imaging for remote sensing and agriculture applications, and he has numerous publications in IEEE conferences. His research interests include image processing, signal processing, communication, machine learning and deep learning.



**G.M.R.I. Godaliyadda** (Senior Member, IEEE) obtained his B.Sc. Engineering degree in Electrical and Electronic Engineering from the University of Peradeniya, Sri Lanka, in 2005, and Ph.D. from the National University of Singapore in 2011. Currently, he is attached to the University of Peradeniya, Faculty of Engineering, Department of Electrical and Electronic Engineering as a Senior Lecturer. His current research interests include image and signal processing, pattern recognition, computer vision, machine learning, smart grid, bio-medical and remote sensing applications and algorithms. He is a Senior Member of the IEEE. He is a recipient of the Sri Lanka President’s Award for Scientific Publications for 2018 and 2019. He is the recipient of multiple grants through the National Science Foundation (NSF) for research activities. His previous works have been published in IEEE-TGRS and several other IEEE-GRSS conferences including WHISPERS and IGARSS. He also has numerous publications in many other IEEE transactions, Elsevier and IET journals and is the recipient of multiple best paper awards from international conferences for his work.



**H.M.V.R. Herath** (Senior Member, IEEE) received the B.Sc.Eng. degree in electrical and electronic engineering with 1st class honours from the University of Peradeniya, Peradeniya, Sri Lanka, in 1998, M.Sc. degree in electrical and computer engineering with the award of academic merit from the University of Miami, USA in 2002, and Ph.D. degree in electrical engineering from the University of Paderborn, Germany in 2009. In 2009, he joined the Department of Electrical and Electronic Engineering, University of Peradeniya, as a Senior Lecturer. His current research

interests include hyperspectral imaging for remote sensing, multispectral imaging for food quality assessment, Coherent optical communications and integrated electronics. Prof. Herath was a member of one of the teams that for the first time successfully demonstrated coherent optical transmission with QPSK and polarization multiplexing. He is a member of the Institution of Engineers, Sri Lanka and The Optical Society. He is a Senior Member of the IEEE. He was the General Chair of the IEEE International Conference on Industrial and Information Systems (ICIIS) 2013 held in Kandy, Sri Lanka. His previous works have been published in IEEE-TGRS and several other IEEE-GRSS conferences including WHISPERS and IGARSS. He received the paper award in the ICTer 2017 conference held in Colombo Sri Lanka. Prof. Herath is a recipient of Sri Lanka President’s Award for scientific research in 2013.



**M.P.B. Ekanayake** (Senior Member, IEEE) received his B.Sc. Engineering degree in Electrical and Electronic Engineering from University of Peradeniya, Sri Lanka, in 2006, and Ph.D. from Texas Tech University in 2011. Currently, he is attached to the University of Peradeniya as a Senior Lecturer. His current research interests include applications of signal processing and system modeling in remote sensing, hyperspectral imaging, and smart grid. He is a Senior Member of the IEEE. He is a recipient of the Sri Lanka President's Award for Scientific Publications in 2018 and 2019.

He has obtained several grants through the National Science Foundation (NSF) for research projects. His previous works have been published in IEEE-TGRS and several other IEEE-GRSS conferences including WHISPERS and IGARSS. He also has multiple publications in many IEEE transactions, Elsevier and IET journals and has been awarded several best paper awards in international conferences.



**D. Jayasundara** received a first-class honors degree in Electrical and Electronic Engineering from University of Peradeniya (2021). He's currently working as an instructor at Department of Engineering Mathematics. His research interests include Mathematics, Deep Learning, Digital Communication and Signal Processing. At present, he is involved in research associated with Hyper-Spectral Imaging for Remote sensing and Applications of Multi-Spectral Imaging.



**L. Ramanayake** graduated with a second-class honors (upper division) degree in Electrical and Electronic Engineering from University of Peradeniya (2021). His research interest includes Machine Learning, Spectral Imaging, High Voltage Engineering and Signal Processing. Currently, he is involved in research associated with Hyper-Spectral Imaging for Identification of Probable Mineral Deposits and Application of Multi-spectral Imaging.



**N. Senarath** received a second-class (upper division) honors degree in Electrical and Electronic Engineering from University of Peradeniya (2021). He's currently working as an instructor at Department of Engineering Mathematics. His research interests include Mathematics, Deep Learning, Digital Communication and Signal Processing. At present, he is involved in research associated with Hyper-Spectral Imaging for Remote sensing and Applications of Multi-Spectral Imaging.



**D. Wickramasinghe** , graduated with a second-class honors (upper division) degree in Electrical and Electronic Engineering University of Peradeniya (2021). His research interests include Machine Learning, Multi-Spectral Imaging and Signal Processing. Currently he is involved in researches related to Hyper-Spectral Imaging for Identification of Probable Mineral Deposits, Potable Water Quality Parameter assessing and Identifying Sugar Adulteration in Black Tea through Multispectral Imaging.